Spall response of single-crystal copper

Turley, W D
Fensin, Saryu Jindal
Hixson, R S
Jones, David Robert
LaLone, B M
Stevens, G D
Thomas, S A
Veeser, Lynn R.

Spall response of single-crystal copper

W. D. Turley, S. J. Fensin, R. S. Hixson, D. R. Jones, B. M. La Lone, G. D. Stevens, S. A. Thomas, and L. R. Veeser

---

Articles you may be interested in

Effect of peak stress and tensile strain-rate on spall in tantalum
Journal of Applied Physics **124**, 085901 (2018); 10.1063/1.5045045

Elastic precursor wave decay in shock-compressed aluminum over a wide range of temperature
Journal of Applied Physics **123**, 035103 (2018); 10.1063/1.5008280

Effect of grain boundaries on shock-induced phase transformation in iron bicrystals
Journal of Applied Physics **123**, 045105 (2018); 10.1063/1.5003891

Dynamic strength properties and alpha-phase shock Hugoniot of iron and steel
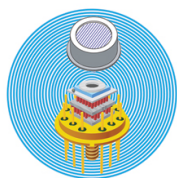Journal of Applied Physics **123**, 175902 (2018); 10.1063/1.5019484

Shock wave propagation and spall failure of nanocrystalline Cu/Ta alloys: Effect of Ta in solid-solution
Journal of Applied Physics **122**, 225901 (2017); 10.1063/1.5001761

Effects of defects and microstructure on release melting of shock-loaded copper: Atomistic simulations
Journal of Applied Physics **123**, 015901 (2018); 10.1063/1.5005000

Spall response of single-crystal copper

W. D. Turley,[1] S. J. Fensin,[2] R. S. Hixson,[3] D. R. Jones,[2] B. M. La Lone,[1] G. D. Stevens,[1] S. A. Thomas,[3] and L. R. Veeser[1,2]
[1]*Nevada National Security Site, Special Technologies Laboratory, Santa Barbara, California 93111, USA*
[2]*Los Alamos National Laboratory, Los Alamos, New Mexico 87545, USA*
[3]*Nevada National Security Site, New Mexico Operations, Los Alamos, New Mexico 87544, USA*

We performed a series of systematic spall experiments on single-crystal copper in an effort to determine and isolate the effects of crystal orientation, peak stress, and unloading strain rate on the tensile spall strength. Strain rates ranging from 0.62 to $2.2 \times 10^6 \, \text{s}^{-1}$ and peak shock stresses in the 5–14 GPa range, with one additional experiment near 50 GPa, were explored as part of this work. Gun-driven impactors, called flyer plates, generated flat top shocks followed by spall. This work highlights the effect of crystal anisotropy on the spall strength by showing that the spall strength decreases in the following order: [100], [110], and [111]. Over the range of stresses and strain rates explored, the spall strength of [100] copper depends strongly on both the strain rate and shock stress. Except at the very highest shock stress, the results for the [100] orientation show linear relationships between the spall strength and both the applied compressive stress and the strain rate. In addition, hydrodynamic computer code simulations of the spall experiments were performed to calculate the relationship between the strain rate near the spall plane in the target and the rate of free surface velocity release during the pullback. As expected, strain rates at the spall plane are much higher than the strain rates estimated from the free surface velocity release rate. We have begun soft recovery experiments and molecular dynamics calculations to understand the unusual recompression observed in the spall signature for [100] crystals. © *2018 Author(s). All article content, except where otherwise noted, is licensed under a Creative Commons Attribution (CC BY) license* (*http://creativecommons.org/licenses/by/4.0/*). https://doi.org/10.1063/1.5012267

I. INTRODUCTION

A material that is compressively shocked and then subjected to tensile strain can incur damage, including spallation and fragmentation. The most common experimental technique (for which the wave interactions are shown in Fig. 1) for generating this condition involves impacting the material of interest (target) with a flyer (impactor) plate. The impact generates shock compression waves in both the target and the flyer plate. These waves, reflected from the free surfaces, generate release waves that interact in the target and cause dynamic tension.

The tensile spall strength for the shocked metal samples has been reported to depend on the crystalline grain structure;[1] the peak compressive stress prior to tension;[2] the shape of the compressive pulse (square or triangular);[3] the dwell time, defined as the time for which the compressive pulse is applied;[4] and the strain rate just before spall.[5] However, previous studies were not designed to determine the independent effects of material properties, peak compressive stress, and tensile strain rate on the measured spall strength. Minich *et al.*,[1] reported a peak compressive stress dependence, but the tensile strain rate was also varied in those experiments, and the relative effects of the two parameters on spall strength were not stated. Similarly, Romanchenko[6] reported a large strain rate dependence for polycrystalline copper, but the shock stress also varied in those experiments. Kanel[7] observed high spall strength with the [111] crystal

orientation and reported values significantly higher than Minich, perhaps because Kanel's impactors were significantly thinner and resultant release rates were high. In those studies, too, the compressive shock strength and tensile strain rate were varied simultaneously, and their individual effects were not isolated.

Minich also found that increasing the grain size increases the spall strength. In fact, the Minich results show an increase in spall strength in single crystals relative to polycrystalline materials, with the highest spall strength observed for the [100] orientation. Presumably, this can be attributed to the lack of grain boundaries in single-crystal samples, which can serve as damage nucleation sites. Likewise, Razorenov[8] and Kanel[7] recorded factors of 2 to 3 increase in spall strength for single crystals relative to polycrystalline copper.

In this study, we have attempted to determine the effects of peak compressive stress and tensile strain rate on the spall strength of single-crystal copper. Most of the experiments are for samples oriented along the [100] direction, but one experiment each for the [110] and [111] orientations was also performed to observe the relative effects of orientation on spall strength. Our main data are from free surface velocity profiles made at the back free surface of the sample. These data provide information regarding the motion of shock waves in a sample and can be used up to a point to infer stresses and kinetics associated with void nucleation and growth. Additional information on the actual spall failure process can be determined using soft recovery
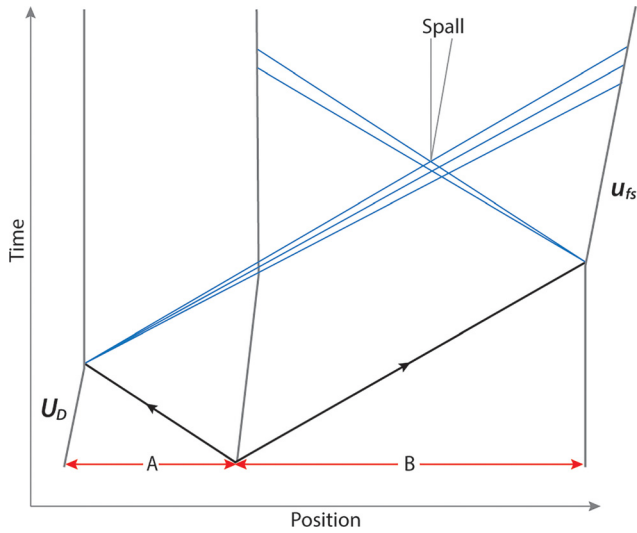
FIG. 1. Time versus position diagram for plate-impactor spall experiments. The shock fronts are black and the release fans are blue. A and B are the impactor and target thicknesses. The inverse slopes of the lines marked U_D and u_{fs} are the impactor and free surface velocities, respectively.

techniques; preliminary metallography results from a [100] sample subjected to a low impact and soft recovered are also discussed. We also present results of molecular dynamics (MD) calculations and propose a model based on crystal orientation plasticity to explain these results.

II. EXPERIMENTAL DESIGN

A flyer plate impact technique was used to generate spall in copper samples. The experiments were conducted using a 40 mm bore, single-stage light gas gun and, in one case, a 40 mm powder gun. A total of thirteen experiments were performed on the three copper orientations, [100], [110], and [111], using different shock-loading impact conditions. Changing the impact velocity changes both the stress state and tensile strain rate, while varying the flyer and target thicknesses affects the tensile strain rate because of rarefaction wave spreading. First, to explore differences caused by crystalline orientation, we performed experiments for each orientation, keeping the impact conditions and material thicknesses nearly identical. Then, a set of [100] experiments was performed where impact velocities and material thicknesses were deliberately varied to change the stress state and tensile strain rate. The key parameters of the experiments are listed in Table I.

All targets and flyers were machined from 99.999% purity copper (MTI Corporation, Richmond, CA). The crystals were prepared with their surface normal oriented in either the [100], [110], or [111] direction and were polished to a specular finish with surfaces that were flat and parallel to within 10 μm. The surface normal was reported by MTI to be within $\pm 2°$ of the selected crystal orientation. The impactors and targets had identical orientations, but only the surface normal directions were oriented; we did not control the relative alignment of the impactor and target. We determined both longitudinal and shear sound speeds using the ultrasonic pulse echo technique, with results for the longitudinal speed (C_L) being [100]

TABLE I. Impactor and target experimental parameters.

Experiment no.	Crystal orientation	Impactor diameter, d_I (mm)	Target diameter, d_T (mm)	Impactor thickness, A (mm)	Target thickness, B (mm)	Impactor velocity, U_D (m/s)
1	[110]	10	10	1.01	2.18	500
2	[111]	10	10	0.99	1.88	502
3	[100]	25	25	1.00	2.04	297
4	[100]	34	25	1.52	3.02	460
5	[100]	25	25	2.04	3.95	598
6	[100]	34	25	2.49	5.00	705
7	[100]	25	25	2.03	3.94	296
8	[100]	25	25	2.03	3.96	280
9	[100]	25	25	1.00	2.05	600
10	[100]	34	25	1.00	2.01	500
11	[100]	10	25	0.50	1.00	284
12	[100]	25	25	1.01	2.04	607
13	[100]	10	10	0.495	1.029	1998

$C_L = 4.417 \pm 0.007$ km/s, [110] $C_L = 5.049 \pm 0.009$ km/s, and [111] $C_L = 5.217 \pm 0.009$ km/s. The results for shear velocity are [100] $Cs = 2.907 \pm 0.006$, [110] $Cs = 2.932 \pm 0.005$ and $Cs_2 = 1.591 \pm 0.003$, and [111] $Cs = 2.166 \pm 0.003$. Uncertainties are greater for shear velocities because of the relatively low signal levels. Note that there are two shear speeds for the [110] orientation. The measured immersion densities, ρ_0, averaged 8.93 g/cm^3 $\pm 0.3\%$.

The free surface velocities of the shocked targets were measured with a 1–2 ns time resolution using photonic Doppler velocimetry[9] (PDV) with two-fiber probes. The impactor velocities were measured using a second PDV with a collimating probe and a beam that passed near the edge of the target.[10] The tilt was 1–2 mrad when it was measured. Experiments 1–12 were fielded on a gas gun at the NSTec Special Technologies Laboratory (STL), and experiment 13 was fielded on a single-stage powder gun at the Lindhurst Laboratory for Experimental Geophysics at Caltech.

III. EXPERIMENTAL RESULTS

A. Impactor velocity measurements

The velocity at which the flyer plate is moving at impact time is a fundamental measured parameter. A PDV system with a collimating probe, as described in Sec. II, made this measurement. The laser beam, estimated to be aligned within 3° of the axis of the launch tube, passed through a hole in the target plate, introducing a cosine error of 0.15%. Because there is little projectile acceleration over the last few centimeters of travel, we were able to analyze the data using large FFT (fast Fourier transform) windows of about 3.3 μs, which gave excellent velocity resolution. Therefore, our uncertainty was dominated by the cosine uncertainty of up to 0.15%. An example projectile velocity record of the end of travel is shown in Fig. 2.

As has been shown in the literature,[11,12] the precision with which this measurement can be done depends upon how the measurement is made and how the data are analyzed. Jensen[11] quotes a precision of about 0.1% for PDV used in this way; our results are comparable with his statement.
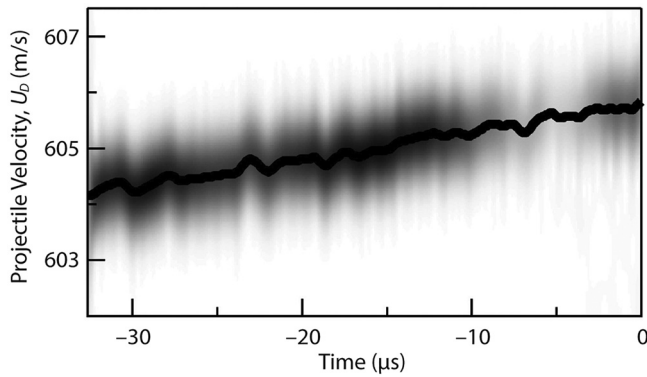
FIG. 2. Example (experiment 12) of the projectile velocimetry spectrogram for the last 2 cm of travel.

B. Free surface velocimetry

First, we performed a set of three experiments on the [100], [110], and [111] orientations, all with very nearly identical shock impact conditions, to determine the dependence of spall response upon orientation. Note that the diameter of the targets and flyers in experiments 1 and 2 was 10 mm, whereas a target diameter of 25 mm and an impactor diameter of 34 mm were used in experiment 10. Computer simulations indicate that edge releases in these experiments were not a problem despite the small target diameters. Figure 3 shows the free surface velocity versus time, u_{fs}, for these experiments. Waveforms for each orientation differ in the rate of release into tension, the magnitude of the pullback velocity, the temporal character of the compressive pulse following spall, and the subsequent ringing.

In the remaining experiments, performed only on the [100] orientation, we systematically varied the impactor velocity and sample thickness to alter the peak stress and tensile strain rate. As mentioned, thicker samples result in lower tensile strain rates (because of wave spreading) for a

given peak stress, whereas higher impact velocities increase both the peak stress and the tensile strain rate. By careful manipulation of target and impactor dimensions, we were able to perform experiments 3, 7, 8, and 11 with peak stress near 5.5 GPa, but with different tensile strain rates. Experiments 5 and 9 had peak stress near 12 GPa and, again, different strain rates. Experiments 6, 7, and 8 had strain rates near $0.1 \times 10^6 \, \mathrm{s}^{-1}$ and experiments 3, 9, and 10 had strain rates near $0.23 \times 10^6 \, \mathrm{s}^{-1}$, both sets for various peak stresses. Finally, we performed experiment 12 with a sapphire window attached to the target free surface to observe the shape of the release wave emanating from the back of the impactor in the absence of spall. Free surface results are shown in Fig. 4 and will be discussed further.

Wave profiles show clear spall signatures that consist of a release into tension, indicated by a velocity decrease, or pullback, with spall occurring at the velocity minimum. Immediately after complete spall (and creation of spall surfaces in the sample), recompression waves propagate in both directions from near the spall plane. In the velocimetry of the
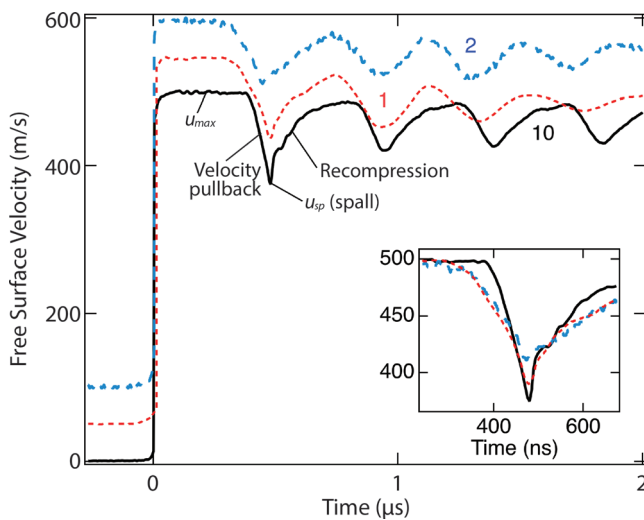

FIG. 3. Free surface velocities for three single-crystal orientations: experiment 1 [110] (red, small dashes); experiment 2 [111] (blue, longer dashes); and experiment 10 [100] (black, solid). The top two traces are offset from zero by multiples of 50 m/s. The inset shows the spall signatures, offset slightly in time for easier comparison of the spall signatures and relative velocity pullbacks.
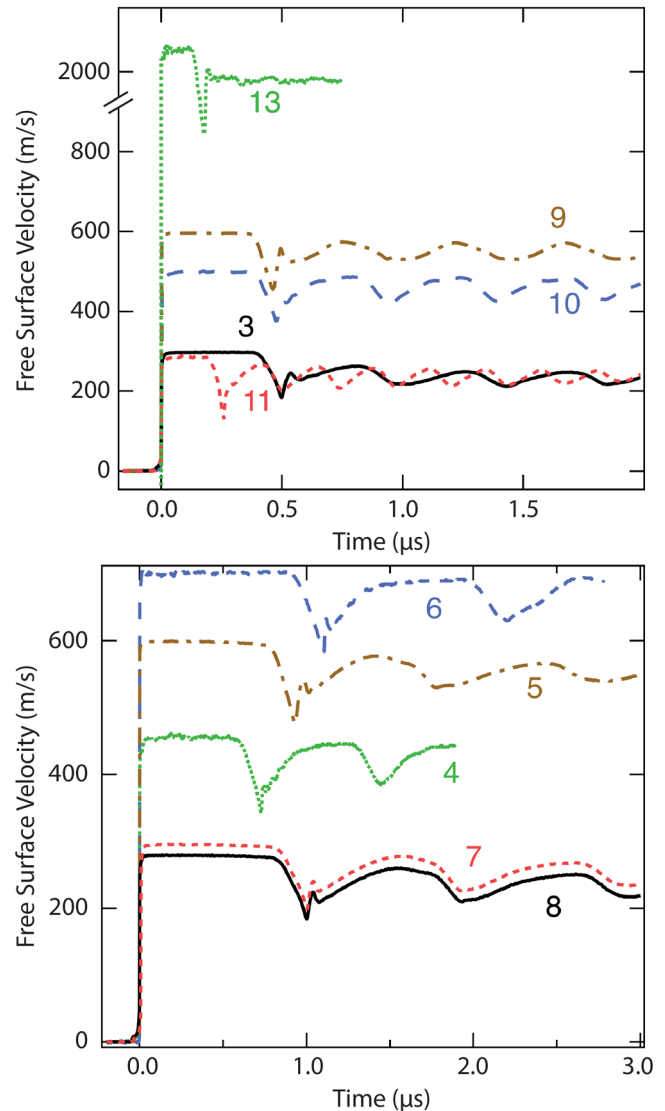

FIG. 4. Wave profiles for experiments done in the [100] orientation for single-crystal copper. The numbers on the plots identify experiments; two graphs are shown to make the results easier to visualize.

free surface, the recompression appears as a velocity increase after spall, and it is followed by ringing in the spall scab. Of interest in the present study are the free surface velocity plateau, u_{max}; the free surface velocity change due to spall, $u_{max} - u_{sp}$ where u_{sp} is the minimum in the free surface velocity just before it increases; the deceleration during velocity pullback (related to the tensile strain rate), $\dot{u}_{fs}$; the shape of the recompression right after the particle velocity minimum; and the ringing in u_{fs} following spall. (A dot above a letter implies the time derivative.) These data can be used to calculate information such as peak stress and spall strength.

IV. CALCULATED PROPERTIES AND DISCUSSION

A. Properties derived from wave profiles

To calculate the peak stress for these experiments, it is important to identify the shock Hugoniot for each orientation. We calculated the peak stress from the momentum conservation equation

$$P_{max} = (1/2)\rho_0 u_{max} U_s, \qquad (1)$$

where U_s is the shock velocity and u_{max} is the peak free surface velocity taken in the steady state after the shock rise. Because of the symmetry and the reflected Hugoniot approximation, u_{max} will be very close to the measured impactor velocity. Although it is possible for each orientation to have a measurably different Hugoniot at these low stress states, we used the polycrystalline shock Hugoniot of Mitchell and Nellis[13] to estimate the peak stress as

$$U_s = S u_p + C, \qquad (2)$$

where $C = 3.933$ km/s is the Hugoniot intercept, $S = 1.50$ is the Hugoniot slope, and u_p is the particle velocity.

For consistency with other shock spall work,[14] the *approximate* spall strength has been calculated using

$$\sigma_{sp} = 1/2\rho_0 C_b(u_{max} - u_{sp}) = 1/2\rho_0 C_b \Delta u_{fs}, \qquad (3)$$

where C_b is the bulk sound speed. This equation ignores Romanchenko's[6] and other small corrections. The *approximate* tensile strain rate in the literature is often calculated from the slope of the release waves (pullback signature) in the free surface velocity record. This is sometimes referred to as the "decompression" strain rate, defined as

$$\dot{\varepsilon} = 1/2(\dot{u}_{fs}/C_b). \qquad (4)$$

This commonly used approximation allows comparison with literature values. Because both Eqs. (3) and (4) are approximations, it is difficult to assign a quantitative uncertainty to either spall strength or strain rate. However, by assuming that their approximate nature is a systematic error, we can still compare the experiment results.

In the current work, we determined the slope of the pullback signal roughly 75 ns before spall. In all experiments, the slope was relatively constant around this time, so the measured decompression strain rates are not very sensitive to the exact time chosen. The intention was to determine the deceleration after quasi-elastic release but shortly before damage begins. Note that with this procedure, the strain rates for the three different orientations are quite similar despite the obvious variations in Fig. 3.

The net result of rarefaction wave spreading is that the tensile strain rate at the spall plane inside the target is much higher than that calculated from the experimental data using the simple definition above. This issue is discussed in more detail in Sec. V, where hydrodynamic computer simulations show that the actual tensile strain rate near the spall plane is roughly six times higher than the definition in Eq. (4). The calculated values for peak stress, approximate spall strength, and approximate tensile strain rate are listed in Table II. Our results are in rough agreement with those of Minich[1] (no tabulated values are given there), as well as with the lower-velocity data of Krishnan *et al.*[15]

TABLE II. Velocities, stress values, and strain rates.

Expt. no.	Crystal orient.	Free surface velocity before spall, u_{max} (m/s)	Peak stress, P (GPa)	Velocity pullback, Δu_{fs} (m/s)	Spall strength, σ_{sp} (GPa)	Deceleration, $\dot{u}_{fs}$ ($10^9 \times$ m/s^2)	Meas. strain rate, $\dot{\varepsilon}_{meas} = \frac{1}{2}$ $(\dot{u}_{fs}/C_b)$ (μs^{-1})[a]	Calc. strain rate, $\dot{\varepsilon}_{calc}$ (μs^{-1})[b]	Ratio of $\dot{\varepsilon}_{calc}$ to $\dot{\varepsilon}_{meas}$
1	[110]	496	9.63	108	1.90	1.56	0.198	–	–
2	[111]	494	9.67	85	1.50	1.06	0.134	–	–
3	[100]	297	5.52	121	2.13	1.82	0.230	1.30	5.6
4	[100]	456	8.80	110	1.94	1.27	0.161	0.95	5.9
5	[100]	598	11.7	120	2.11	1.02	0.129	0.75	5.8
6	[100]	701	14.1	118	2.08	0.81	0.103	0.62	6.0
7	[100]	294	5.50	95	1.67	0.83	0.105	0.65	6.2
8	[100]	279	5.19	96	1.69	0.81	0.103	0.70	6.8
9	[100]	595	11.8	147	2.59	1.90	0.241	1.5	6.2
10	[100]	498	9.63	124	2.18	1.82	0.231	1.4	6.1
11	[100]	286	5.26	157	2.76	4.07	0.516	2.2	4.3
12	[100]	595	11.9	NA	NA	0.97[c]	NA	–	–
13	[100]	2036	49.6	209	3.68	5.51	0.700	3.8	5.4

[a]Determined from the measured free surface velocity about 75 ns before spall. We took the bulk sound speed to be $C_b = 3.93$ km/s.
[b]Calculated at the spall plane at the time when the stress release first goes into tension there.
[c]Window interface deceleration, not free surface.

The part of the wave profile around spall derives from the reflected wave returning from the back of the flyer plate but modified by interactions with the release wave from the target free surface. The resulting wave, which carries information about the spall process, then spreads as it moves from the spall plane out to the free surface, where the time-resolved measurements are made. To study the effects of these wave interactions on the measured free surface profile, we configured experiment 12 with a sapphire window attached to the back surface of the target to reduce the amplitude of the release wave generated at the target free surface. Other parameters for this experiment were similar to those of experiment 9. The objective was to prevent spall and thereby greatly reduce the perturbations through which the wave reflected from the impactor passes on its way to the observed target surface. Figure 5 shows the particle velocity of the sample–window interface for experiment 12 and the approximate particle velocity ($^1/_2 u_{fs}$) for experiment 9. To correct for the mismatch of shock impedance between the sample and window, making it easier to compare the release rates in the figure, we multiplied particle velocities from experiment 12×1.07. As seen in Fig. 5, the release rates near 4.5 μs are identical within a few percent, indicating that the spall perturbations do not have a large effect on the release rate in this case.

B. Different crystal orientations with similar shock conditions

This section presents further results for the three initial experiments (1, 2, and 10) in which crystalline orientations were studied at very close to the same impact conditions (Fig. 3). The highest spall strength was measured for the [100] orientation, with slightly smaller values recorded for the [110] and [111] orientations, respectively. Note from Fig. 3 that the ringing amplitudes decayed faster for the [110] and [111] crystals as compared to the [100] crystal. The period of ringing following spall can be used to estimate the physical location of the spall plane in the target. For

experiment 10, the period is $T \sim 460$ ns, which indicates a spall scab thickness about $^1/_2 TC_L \sim 1.02$ mm, consistent with the impactor and target thicknesses of ~ 1.0 and 2.0 mm, respectively. The differing decay rates is a topic for further research.

Also note that it is clear from Fig. 3 that release from the peak stress state occurs sooner for [110] and [111] orientations than for [100], which is due to the different elastic sound speeds, see Sec. II. Consequently, the [110] and [111] quasi-elastic release waves will arrive earlier than for the [100] orientation.

C. Varying shock stresses and strain rates for [100] crystals

Experiments 3–13 were performed on [100] copper, and the goal was to study the effects of peak shock stress and strain rate on spall behavior. The details of the peak stresses and strain rates are listed in Table II and the wave profiles are shown in Fig. 4. In addition, Table II lists the parameters derived in the data analysis, including shock velocity, peak stress, pullback velocity, spall strength, and strain rate.

For the initial study of spall strength, we neglected experiment 13, which was done for a much higher shock stress, and experiment 12, done with a sapphire window. Figure 6 shows spall strengths for the remaining [100] experiments, experiments 3–11, as a function of strain rate and peak shock stress. There is a clear dependence of spall strength on the strain rate, but there is considerable scatter. For the plot of approximate spall strength with peak compressive stress, there is a great deal of scatter at low stress.

Because we were unable to describe the spall strength adequately as a function of only compressive stress or strain rate, data were fit to the simplest function that includes both variables

$$\sigma_{sp} = \kappa_0 + \kappa_1 P + \kappa_2 \dot{\varepsilon}. \tag{5}$$

Surprisingly, all data are well fit by a single plane, as shown by Fig. 7, indicating that the spall strength in the ranges evaluated is linearly dependent on both the peak compressive stress and the strain rate. The parameters in Eq. (5) were calculated to be

$$\kappa_0 = 0.97\,(19)\,(\text{GPa}),$$
$$\kappa_1 = 0.05\,(1), \quad \text{and}$$
$$\kappa_2 = 0.66\,(9)\,(\text{GPa}\,\mu\text{s}).$$

After the 49.6 GPa data from experiment 13 were included, a planar fit was no longer adequate to describe the measurements. Consequently, for more extreme conditions, Eq. (5) does not hold, and more data will be required to determine the exact dependence of spall strength in such cases.
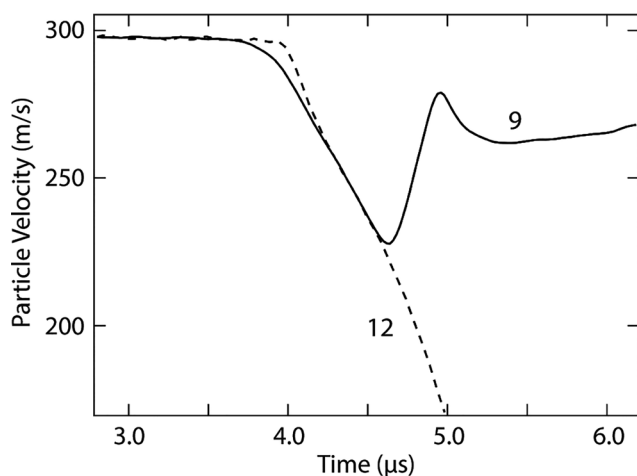
FIG. 5. Spall experiment 9 (solid) and window experiment 12 (dashed) with similar shock parameters. For [100] crystals, the complex multiwave interaction at the spall plane has at most a small effect on the release wave transmitted to the free surface.

D. Rapid recompression signature for [100] orientation

The spall signature of the [100] copper crystals is unique in that after the minimum in free surface velocity, there is a
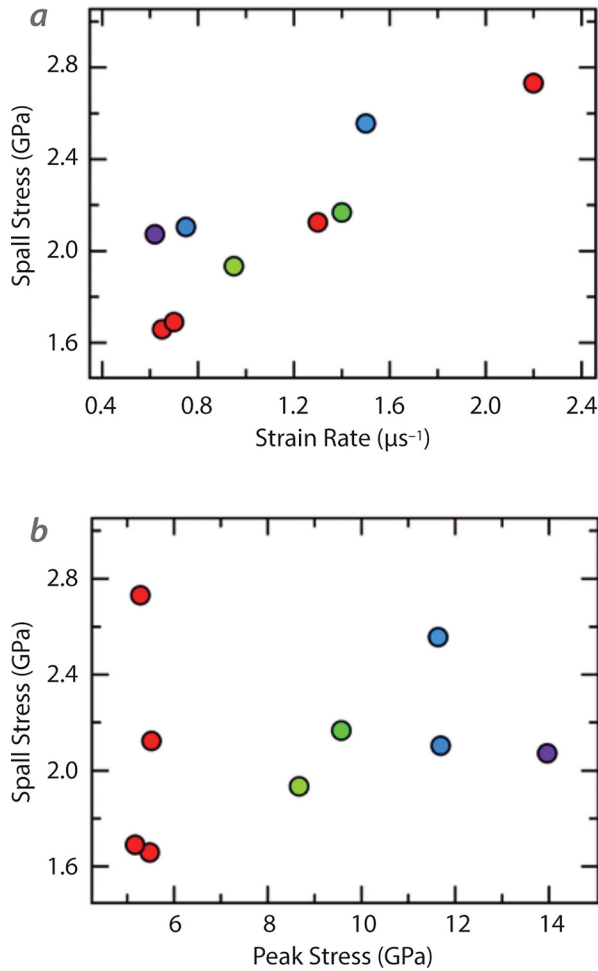
FIG. 6. (a) Spall strength versus CTH-calculated strain rate and (b) versus peak stress. The points are rainbow color-coded with increasing peak stress as seen in (b). The large amount of scatter in the data when plotted this way is evidence that both peak stress and strain rate affect the spall strength.

FIG. 7. [100] oriented copper spall stress as a function of peak compressive stress, *P*, and the CTH calculated strain rate. The green spheres are our data. A minimized chi-squared fit to a single plane accurately fits all of the data except high-stress experiment 13 (not shown). The slopes of the plane relative to *P* and $\dot{\varepsilon}$ can be seen in (a), and deviations from the plane are apparent in (b). When we substituted the strain rate values from the measured velocity release rates using Eq. (4), we obtained fits of similar quality.

very sudden and rapid compressive pulse, followed by another decrease in particle velocity at about its previous rate, followed by fast ringing. A similar "hiccup" feature was observed by Minich,[1] also mainly for [100] crystals. This contrasts a much more gradual compressive pulse from the spall plane in polycrystalline copper. In Minich,[1] other orientations of single-crystal copper sometimes show a feature there as well, but one that is much less distinct.

Figure 8 shows the spall pulse for experiment 7 on [100] copper. Also shown is the spall signature for a polycrystalline experiment with impactor velocity V = 303 m/s, and target dimensions A = 2.004 mm and B = 3.91 mm.[16] The "hiccup" feature in the [100] data is not observed in polycrystalline data. It is postulated here that it is due to the order and symmetry that exists in the [100] orientation, but the origins of this feature are clearly of interest. We performed initial MD simulations and metallurgical analysis on soft-recovered samples to investigate the root cause of this feature; these simulations are discussed in Sec. VI.

V. HYDRODYNAMIC COMPUTER SIMULATIONS

Experimental measurements of the free surface velocity provide a great deal of information about spall, but the actual
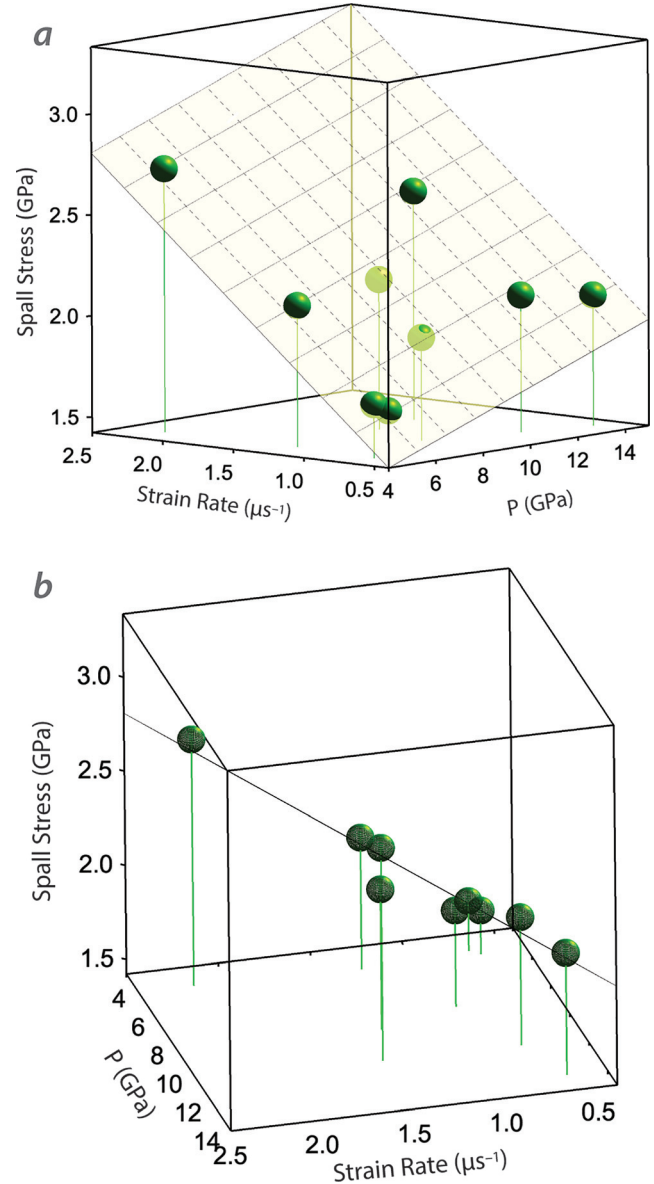
spall process takes place earlier, within the sample, so any observed waves must have propagated from the spall plane to the surface. To better understand the actual spall process and especially the tensile release rate at the spall plane, we performed numerous computer simulations with the Eulerian hydrodynamic code CTH.[17] First, agreements between the calculations and the measured free surface velocity were optimized. Then, the calculated stress and plastic strain rate (PSR) were determined in the region near the spall plane around the time when the stress releases through zero. The time when the sample first goes into tension was chosen because it is when damage (voids) can begin to form. In the calculations, the PSR is nearly constant, or at least does not change rapidly, for distances of tens of calculational cell
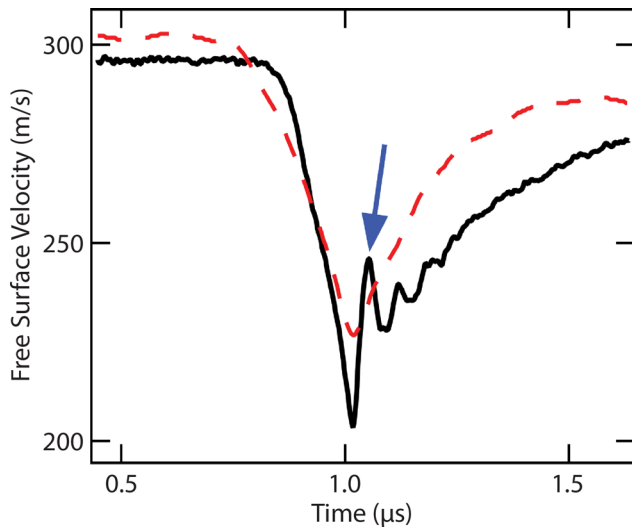
FIG. 8. Free surface velocity of experiment 7 (black, solid) showing recompression after spall with spike "hiccup," indicated by the blue arrow, and subsequent fast ringing. This behavior is characteristic of all [100] spall experiments, and it is present but less distinct for the other orientations. For comparison, a polycrystalline experiment (red, dashes) from another (unpublished) experiment is shown with a slightly higher impactor speed. Similar [100] spall signatures may be compared with those for polycrystalline copper in Minich.[1]

thicknesses (a cell is $\geq 2\,\mu m$ wide) on either side of the spall plane. Likewise, the PSR varies slowly with time for times of a few tens of nanoseconds before spall.

Table II gives the simulated PSR values and, for comparison, the strain rates calculated from Eq. (4) using the free surface deceleration measured ~75 ns before spall. An interesting conclusion is that the simulated strain rate near the spall plane is consistently about 6 times the calculated strain rate from the free surface deceleration for our conditions (the target is twice as thick as the impactor). This disparity results from both the wave interaction between release waves and the spreading of the release rarefaction waves as they propagate from the spall plane to the target free surface. Simulations show that pressure decay rates of the release waves from both the impactor and target are important for determining the tensile strain rate at the spall plane. This difference between the stain rate measured at the free surface and that which occurs within the sample has long been known,[18] but the perturbations were very difficult to keep track of until high-speed computers and good hydrodynamic codes were available.

VI. MOLECULAR DYNAMICS SIMULATIONS AND SOFT-RECOVERY EXPERIMENT

Molecular dynamics simulations were used to gain insights into the "hiccup" that is observed during recompression in the spall signal for the [100] orientation. To understand the origins of the observed discontinuity in the spall signature of [100] copper, we investigated the mechanisms that drive damage and failure in two different orientations, [100] and [111]. Note that MD views the relevant processes at much smaller length and time scales and with strain rates around $10^{10}\,s^{-1}$, much higher than those seen in our

continuum level measurements. Details of the simulation methodology are provided elsewhere.[19,20]

MD results show that under initial shock compression in the stress regime from 25 to 40 GPa, the [100] orientation undergoes plastic deformation, whereas no plasticity is observed in the [111] crystal; see Fig. 9. For the simulations, the crystals were assumed perfect and without defect; it has been shown previously that the initial defect density can have an impact on the magnitude of the wave structure, especially the Hugoniot elastic limit.[21] In general, all "real" materials have an initial equilibrium defect density. As these defects are not included in our simulations, dislocations must actually nucleate in the calculated system. The pre-existing defects in real materials lower the threshold for dislocation nucleation and motion, which is associated with plastic deformation. In fact, previous simulation work by Germann *et al.*,[22] shows that in these perfect crystals the elastic precursor is overdriven in the [100] orientation (because yield occurs at a lower stress) but is observed in the [111] and [110] orientations. This is consistent with results shown in Fig. 9, where the simulations show that it *is easier to nucleate dislocations* in the [100] orientation than the [111].

The current calculations agree with previous studies that show that [111] crystals have higher compressive strength than [100] crystals.[22] Earlier simulations of copper bicrystals show that increased plastic deformation under compression can increase the spall strength because the deformation relaxes some of the applied shear stress, making it much harder for the material to reach the critical void nucleation stress.[20] Hence, plasticity under compression can be an important stress dissipation mechanism.

Furthermore, these MD results agree with indirect experimental findings showing that grain boundaries surrounded by "softer" grains, as defined by the Schmid factor, tend to not nucleate voids as easily as boundaries surrounded by "harder" grains. Softer grains promote plasticity and harder grains retard it. The Schmid factor is a measure of the ease with which plastic deformation can occur; therefore, these experimental results, along with others,[24] indirectly verify the findings from MD simulations. Consistent with this, the present MD simulations show that a few large voids are nucleated in [100] orientation compared to a large number of small voids in the [111] orientation. This suggests that the damage mechanism is *growth* dominated in [100] and
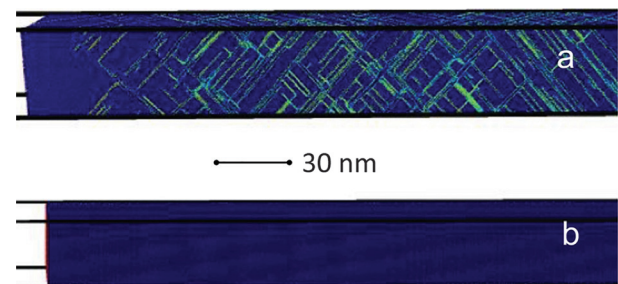

FIG. 9. Simulation cells corresponding to (a) [100] and (b) [111] crystals under shock compression. The calculations were done for particle velocities of 750 m/s. The atoms are colored by the centrosymmetry parameter, where the blue atoms represent the perfect face-centered cubic (FCC) lattice and green indicates atoms no longer in an FCC state.

nucleation dominated in the [111] orientation, as shown in Fig. 10. The few voids that nucleate in [100] initially grow at a fast rate because [100] is a softer orientation, and void growth rates depend on the ability of the surrounding matrix to plastically deform.[23] In contrast, many small voids nucleate in the [111] orientation but grow more slowly than in the [100] orientation. This observation from MD is also in qualitative agreement with the PDV data in Fig. 3 and spall strength data in Table II. The experimental data show that the [100] orientation has a higher spall strength coupled with a steeper slope in the recompression (snap-back) signal than the [111] orientation.

These MD results may provide an explanation for the hiccup in the spall signal of the [100] orientation. It has been shown for single-phase brittle[24] and ductile[25] materials that the rate at which the recompression velocity rises after spall can be directly correlated to the rate of void growth. A faster velocity increase (steeper slope) can be correlated with a higher void growth rate. Later, when the material is saturated with dislocations, there will be a slowing in the growth rate. So the hiccup in the pullback signal can be interpreted as an initial fast void growth rate in the [100] orientation, which eventually slows down when the damage has saturated in the matrix. Precisely how these dynamic mechanisms manifest themselves in the observed free surface velocity record, and if agreement with data is seen, requires more research.

Soft-recovery, low-stress impactor plate experiments are in progress for the [100] and [111] orientations to obtain

further evidence for this hypothesis. Shown in Fig. 11 are the preliminary results for very low–impact stress conditions (90 m/s with Z-quartz flyer, ~1 GPa) in the [100] orientation. These conditions are well below the threshold for spall. Metallography results show the morphology of the nucleated voids in Fig. 11. The voids in the [100] crystal are diamond shaped and their long axes are aligned with the [100] direction. These results show a 2-D cross section of octahedral voids with their faces lying on each of the four {111} slip systems available in the [100] orientation in copper. Similar results have been observed previously in shock-loaded copper bi-crystals.[26] While this observation is interesting and shows the deformation along the {111} slip planes at 45° to the [100] loading direction, additional work is required to validate the premise. Results of a more complete set of recovery experiments will be reported in a future article.

VII. SUMMARY

We have done dynamic experiments to measure the tensile response of polycrystalline and single-crystal copper in three orientations, [100], [110], and [111]. This work was motivated by a desire to better understand how the dynamic damage process works in single-crystal copper when there are no grain boundaries to aid the nucleation of the damage process and by the desire to determine the role of crystalline anisotropy.

In this work, the [100] orientation has a higher spall strength than polycrystalline and the other orientations studied; this result agrees with previous studies from Minich *et al.*[1] Another result is that for [100] single crystals, the spall strength depends strongly upon both the initial compressive stress prior to the onset of tension and the tensile strain rate. The dependence on both parameters is very close
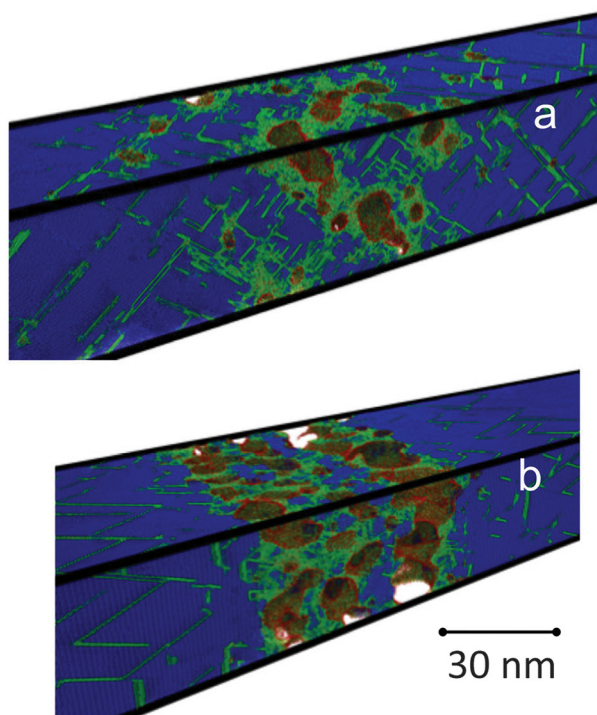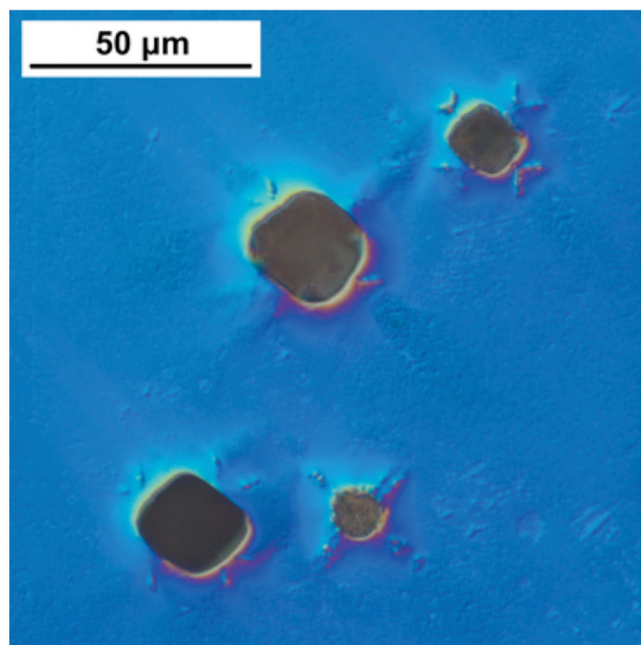

FIG. 10. Simulation cells corresponding to (a) [100] and (b) [111] crystals during spall. The calculations were done for particle velocities of 750 m/s. The atoms are colored by the centrosymmetry parameter where the blue atoms represent the perfect FCC lattice and green and other colors indicate atoms no longer in an FCC state; brown and white indicate increased centrosymmetry. The colored atoms highlight stacking faults and plastically deformed regions.

FIG. 11. Diamond-shaped voids in the [100] sample, with both the [100] direction and shock direction vertical in this image. Also visible are primary slip planes at 45°. The surface has been lightly etched to enhance the surface features under differential interference contrast illumination.

to linear over the peak stress range from 4 to 14 GPa and tensile strain rates from 0.6 to $2.2 \times 10^6 \, \text{s}^{-1}$ at the spall plane (which correspond to approximate strain rates of 0.1 to 0.5 at the free surface). Plotting the spall strength as a function of both parameters shows that they fall on a plane to a very good approximation. The spall strength from a high-stress (50 GPa) experiment did not lie on the plane, suggesting a limited range of the linear dependence.

In dynamic spall experiments, formation of the spall surface is indicated by the initial velocity increase when the new surface snaps back upon release of tension. In our study, the spall signature of the [100] copper crystals is unique in that after the minimum in free surface velocity, there is often a very sudden and rapid velocity increase. The rate of increase is higher than in polycrystalline copper and the other orientations studied. This signature is evidence that spall formation is more rapid in [100] copper.

MD simulations were performed to help understand the differences in tensile damage observed between the [100] and other crystal orientations. These simulations indicate a higher density of dislocations under compression and a higher threshold of void formation in the [100] orientation relative to the [111] orientation. Furthermore, the simulations show that spall along the [100] orientation in copper is characterized by relatively few voids and rapid void growth, while in the [111] orientation, spall formation is characterized by nucleation of many voids and slow void growth. This is consistent with the experimental observations of a higher spall strength and a more rapid spall surface formation for the [100] orientation.

Metallurgical examination of the recovered [100] sample from a shock below spall reveals that, as seen by Perez-Bergquist *et al.*,[26] the voids for the [100] direction are diamond shaped because of the orientation of the primary slip systems to the shock propagation directions. More recovery experiments, with increasing impact stress levels, will be done in the future to look for differences in void densities and details of the complete failure process.

ACKNOWLEDGMENTS

[1] R. W. Minich, J. U. Cazamias, M. Kumar, and A. J. Schwartz, Metall. Mater. Trans. A **35**, 2663 (2004).

[2] T. Antoun, L. Seaman, D. R. Curran, G. I. Kanel, S. V. Razorenov, and A. V. Utkin, in *Spall Fracture*, edited by L. Davison and Y. Horie (Springer, New York, 2003), Section 4.2.

[3] G. T. Gray III, N. K. Bourne, B. L. Henrie, and J. C. F. Millett, J. Phys. IV (France) **110**, 773 (2003); R. S. Hixson, G. T. Gray, P. A. Rigg, L. B. Addessio, and C. A. Yablinsky, AIP Conf. Proc. **706**, 469 (2004); D. D. Koller, R. S. Hixson, G. T. Gray III, P. A. Rigg, L. B. Addessio, E. K. Cerreta, J. D. Maestas, and C. A. Yablinsky, J. Appl. Phys. **98**, 103518 (2005).

[4] A. K. Zurek and M. A. Meyers, in *High Pressure Shock Compression of Solids II: Dynamic Fracture and Fragmentation*, edited by L. Davison, D. E. Grady, and M. Shahinpoor (Springer, New York, 1996), p. 25.

[5] J. N. Johnson, G. T. Gray III, and N. K. Bourne, J. Appl. Phys. **86**, 4892 (1999).

[6] V. I. Romanchenko and G. V. Stepanov, J. Appl. Mech. Tech. Phys. **21**, 555 (1980).

[7] G. I. Kanel, S. V. Rasorenov, and V. E. Fortov, in *Shock-Wave and High-Strain-Rate Phenomena in Materials*, edited by M. A. Meyers, L. E. Murr, and K. P. Staudhammer (Marcel Dekker, New York, 1992), p. 775.

[8] S. V. Razorenov, G. I. Kanel, and V. E. Fortov, Sov. Phys. Dokl. **35**, 976 (1990).

[9] O. T. Strand, D. R. Goosman, C. Martinez, T. L. Whitworth, and W. W. Kuhlow, Rev. Sci. Instrum. **77**, 083108 (2006).

[10] The collimated probe returns reflected light from the sample to the input fiber. It is used when we need to follow a surface over a long distance. The two-fiber probe has separate input and collection fibers and no focusing lens. Consequently its efficiency drops off quickly with distance from the sample surface, and its dynamic range is relatively small. We use two-fiber probes primarily where there is a risk of losing the data if the surface tilts or bends upon being shocked.

[11] B. J. Jensen, D. B. Holtkamp, P. A. Rigg, and D. H. Dolan, J. Appl. Phys. **101**, 013523 (2007).

[12] D. H. Dolan, Rev. Sci. Instrum. **81**, 053905 (2010).

[13] A. C. Mitchell and W. J. Nellis, J. Appl. Phys. **52**, 3363 (1981).

[14] Antoun, op. cit., p. 95.

[15] K. Krishnan, A. Brown, L. Wayne, J. Vo, S. Opie, H. Lim, P. Peralta, S.-N. Luo, D. Byler, K. J. McClellan, A. Koskelo, and R. Dickerson, Metall. Mater. Trans. A **46**, 4527 (2015).

[16] S. A. Thomas *et al.*, "Shock dwell time effects in copper spall" (to be published).

[17] J. M. McGlaun, S. L. Thompson, and M. G. Elrick, Int. J. Impact Eng. **10**, 351 (1990); E. S. Hertel, Jr., R. L. Bell, M. G. Elrick, A. V. Farnsworth, G. I. Kerley, J. M. McGlaun, S. V. Petney, S. A. Silling, P. A. Taylor, and L. Yarrington, in *Shock Waves @ Marseille*, edited by R. Brun and L. Z. Dumitrescu (Springer Press, 1995), p. 377.

[18] I. C. Skidmore, Appl. Mater. Res. **4**, 131 (1965).

[19] S. J. Fensin, S. M. Valone, E. K. Cerreta, and G. T. Gray III, J. Appl. Phys. **112**, 083529 (2012).

[20] S. J. Fensin, E. K. Cerreta, G. T. Gray III, and S. M. Valone, Sci. Rep. **4**, 1 (2014).

[21] R. Ravelo, B. L. Holian, and T. C. Germann, AIP Conf. Proc. **1195**, 825 (2010).

[22] T. C. Germann, B. L. Holian, P. S. Lomdahl, and R. Ravelo, Phys. Rev. Lett. **84**, 5351 (2000).

[23] R. A. Lebensohn, J. P. Escobedo, E. K. Cerreta, D. Dennis-Koller, C. A. Bronkhorst, and J. F. Bingert, Acta Mater. **61**, 6918 (2013).

[24] J. P. Escobedo, E. N. Brown, C. P. Trujillo, E. K. Cerreta, and G. T. Gray III, J. Appl. Phys. **113**, 103506 (2013).

[25] S. Cochran and D. Banner, J. Appl. Phys. **48**, 2729 (1977).

[26] A. G. Perez-Bergquist, E. K. Cerreta, C. P. Trujillo, F. Cao, and G. T. Gray III, Scr. Mater. **65**, 1069 (2011).